Materials & Design 220 (2022) 110876

Contents lists available at ScienceDirect

Materials & Design

journal homepage: www.elsevier.com/locate/matdes

Tailoring strain-hardening behavior of high-strength Engineered Cementitious Composites (ECC) using hybrid silica sand and artificial geopolymer aggregates

Ling-Yu Xu, Bo-Tao Huang *, Jian-Cong Lao, Jian-Guo Dai *

Department of Civil and Environmental Engineering, The Hong Kong Polytechnic University, Hong Kong, China

HIGHLIGHTS

- Strain-hardening behavior of Engineered Cementitious Composites (ECC) can be tailored by hybridization of geopolymer aggregates (GPA) and silica sand.
- GPA substitution improves the tensile ductility, crack resistance, and energy absorption of ECC.
- Introducing GPA in ECC matrix results in more active flaws and saturated multiple cracking.

GRAPHICAL ABSTRACT

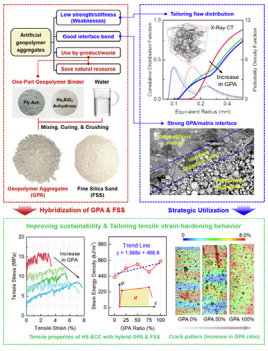

ARTICLE INFO

Article history:
Received 4 December 2021
Revised 16 May 2022
Accepted 18 June 2022
Available online 21 June 2022

Keywords:
Artificial aggregate
Geopolymer aggregate
Alkali activated
Engineered Cementitious Composites (ECC)
Strain-Hardening Cementitious Composites (SHCC)
Ultra-High-Performance Concrete (UHPC)
X-ray CT

ABSTRACT

Hybrid artificial geopolymer aggregates (GPA) and natural silica sand were used to strategically tailor the tensile strain-hardening behavior of high-strength engineered cementitious composites (HS-ECC). With such hybridization, the weaknesses of GPA (i.e., relatively low strength and stiffness) were utilized in the performance-based design of HS-ECC, while the advantages of GPA were retained (e.g., the utilization of industrial by-products/wastes through chemical activation and conservation of natural resources). In this study, a comprehensive experimental program was conducted at multiple scales on the HS-ECC. It was found that increasing the replacement ratio of silica sand by GPA improved the tensile ductility, crack control ability, and energy absorption of HS-ECC, although its compressive and tensile strengths were reduced. GPA with low alkalinity were observed to react with the cementitious matrix, and the pozzolanic reaction provided additional chemical bond and thus enhanced the GPA/matrix interface. In addition, GPA could be regarded as "additional flaws" in the HS-ECC system. According to the Weibull-based modeling, it was found that GPA could play a crack-inducing role in activating more inactive initial flaws. Therefore, GPA can tailor the active flaw size distributions in HS-ECC matrix. The findings of this study provide a new avenue for the utilization of GPA.

1. Introduction

The concrete technology develops rapidly in recent decades. Due to the brittleness of concrete materials, one of the major trends is to develop highly ductile cementitious composites. A rep-

* Corresponding authors.
E-mail addresses: ling-yu.xu@connect.polyu.hk (L.-Y. Xu), botaohuang@zju.edu.cn (B.-T. Huang), jiancong.lao@polyu.edu.hk (J.-C. Lao), cejgdai@polyu.edu.hk (J.-G. Dai).

https://doi.org/10.1016/j.matdes.2022.110876
0264-1275/

resentative of such advanced fiber-reinforced cementitious materials is "Engineered Cementitious Composites" (ECC) [1,2,3], also known as "Strain-Hardening Cementitious Composites" (SHCC) [4,5,6] or "Ultra-High-Toughness Cementitious Composites" (UHTCC) [7,8]. ECC possess outstanding tensile strain capacity which is several hundred times (typically 300–1000 times) that of the ordinary concrete. Owing to the tensile strain-hardening and multiple-cracking characteristics, ECC can exhibit fine cracks under monotonic, cyclic, and even impact loadings. In addition, with the combined use of a dense matrix and high-strength high-modulus fibers [e.g., polyethylene (PE) fiber], ECC can be produced with a high/ultra-high compressive strength of 100–210 MPa [9,10,11,12], which is similar to that of ultra-high-performance concrete (e.g., [13,14,15,16]). The outstanding performances of the high-strength ECC make it a more promising material for developing durable and resilient civil infrastructures.

Many efforts have also been made to develop greener ECC, by improving the sustainbablity of binder materials, fiber reinforcements, and fine aggregates. Industrial/urban by-products/wastes are used as aggregates in ECC to replace the commonly-used fine silica sand, because the production of the latter consumes significant natural resources and energy. For normal strength ECC (e.g., compressive strength < 70 MPa), several available grain-like by-products/wastes have been used to replace silica sand, including bottom ash [17], iron ore tailings [18,19], recycled concrete fragments [20,21], sugarcane bagasse ash [22], waste glass [23,24], and crumb rubber [25,26]. In addition, coarse river sand [27] and sea-sand [28,29] have also been used to fully replace fine silica sand for the development of cost-effective high-strength (HS-ECC) (i.e., 70 ∼ 120 MPa) and ultra-high strength ECC (i.e., >120 MPa).

Use of artificial aggregates through the cold-bonding technology for the production of concrete is an emerging technology. This technology has become more and more attractive. It has gradually been transferred from the laboratory study to the industrial applications due to the unprecedent construction activities and an increasing emphasis on the sustainability issue of construction. It is noted that the source materials for artificial aggregates can be powder-like by-products/wastes widely available from the urban, industrial and agricultural fields. Therefore, the artificial aggregate technology not only saves the limited natural silica rock resources, but also reduces the environmental burden of increasing urban/industrial wastes [30,31]. Among existing artificial aggregates, geopolymer aggregates (GPA) can be produced from aluminosilicate-rich sources by the method of alkali/acid activation [32,33]. Similar to geopolymer pastes, the strength of GPA mainly comes from the three-dimensional cross-linked sodium/potassium-aluminum–silicate-hydrogen (N-A-S-H/K-A-S-H) gels. Considering that geopolymer materials can have a strength similar to that of cement pastes, and exhibit excellent bond with the cement-based matrix, GPA have a potential to be used as a substitution of natural aggregates in concrete production [34].

It should be noted that the cold-bonding GPA inevitably have an inferior strength and a more porous microstructure than natural aggregates, which may pose a concern on the strength and durability of geopolymer aggregate concrete. Therefore, at present, GPA may just be considered for use in roadbed materials in pavement engineering or in nonstructural concrete members [32]. The authors' recent study has revealed that in HS-ECC materials, it is possible to use GPA to replace fine silica sand for improved ductility, and GPA is more suitable than artificial cement-bonded aggregates for the production of high-strength high-ductility ECC [33]. For normal-strength ECC, the aggregates can influence the tensile ductility through the effects on matrix fracture toughness, cracking strength, and modulus [35,36]. However, the unique feature of GPA would show a different influence from that of natural aggregates on ECC performance. Therefore, in another study of the authors, ECC with different GPA-to-binder ratios were investigated to understand the preliminary mechanism of GPA in ECC. It was found that different from fine silica sand (FSS) used in ECC, GPA can be regarded as "additional flaws" in high-strength ECC matrix [34]. The aforementioned work inspired the authors that GPA may be an ideal modifier for ECC materials to tailor tensile ductility and to improve sustainability simultaneously. In addition, once GPA is used as a modifier, the understanding of the interaction between initial flaw and GPA is critical for the performance-based design. Certainly, the advantages of GPA such as the utilization of by-products/wastes and the environmental friendliness remain unchanged.

Thus, in this study, the authors explored the feasibility of using hybrid silica sand and GPA to tailor the mechanical performance of high-strength ECC. The major aims are to study how the replacement ratio of fine silica sand by GPA influence the performance of HS-ECC in terms of the compressive/tensile strength, tensile strain-hardening behavior, and crack evolution. The underlying mechanisms were also clarified through various levels of analyses [e.g., Scanning Electron Microscope (SEM), Digital Image Correlation (DIC), X-ray Computed Tomography (XCT)] and theoretical modeling. The findings of this work provide an innovative performance-based design approach for ECC materials and an in-depth understanding of the interaction between initial flaw and GPA.

2. Experimental programs

2.1. Raw materials

Coal fly ash (FA) provided by China Light & Power Co. Ltd, Hong Kong was used as the precursor for GPA production. Type I 52.5 N Portland cement purchased from Green Island Cement Co. Ltd., and silica fume (SF) transported from Mainland China were used as the binder materials for ECC casting. The chemical components of these raw materials were obtained from X-ray Fluorescence (XRF) analysis as summarized in Table 1 in oxide expressions. From the table, the FA used in the study can be regarded as Class F Fly Ash with the total content of SiO_2, Al_2O_3 and Fe_2O_3 (79.49%) higher than 50%, the CaO content (9.14%) less than 18%, and LOI (2.90%) less than 6% according to ASTM C618-19 [37]. The morphologies of these raw materials are shown in Fig. 1.

Anhydrous sodium metasilicate (Na_2SiO_3-Anhydrous) particles in industrial grade purchased from Qingdao Haiwan Chemical Co., Ltd. were taken as the solid activator for GPA production. According to the product information provided by producers, the chemical compositions of the Na_2SiO_3-Anhydrous particles were 50.75% Na_2O, 46.52% SiO_2, and 2.73% impurities with a silica modulus ratio [i.e., Mol (SiO_2) / Mol (Na_2O)] of 0.94. The particle sizes of

Table 1
Chemical components of raw materials obtained from XRF.

Chemical composition	FA	Cement	SF
Aluminum oxide, Al_2O_3	26.90%	6.07%	0.15%
Silicon oxide, SiO_2	43.40%	19.60%	96.90%
Calcium oxide, CaO	9.14%	64.80%	0.53%
Ferric oxide, Fe_2O_3	9.19%	3.01%	0.06%
Magnesium oxide, MgO	3.49%	0.87%	1.10%
Sulfur trioxide, SO_3	1.65%	4.24%	0.12%
Titanium dioxide, TiO_2	0.91%	0.26%	–
Sodium oxide, Na_2O	3.16%	–	–
Phosphorus oxide, P_2O_5	0.44%	0.13%	0.33%
Potassium oxide, K_2O	1.28%	0.68%	0.78%
Others	0.44%	0.34%	0.03%
LOI (950 °C)	2.90%	3.83%	1.78%

the Na_2SiO_3-Anhydrous particles were between 0.25 mm and 1 mm, and the loose bulk density was 1.31 g/cm^3.

Fine silica sand (FSS) with an average particle size smaller than 300 μm was used for aggregate hybridization. According to GB/T 14684–2011 [38], the water absorption and specific gravity of FSS were tested as 0.8% and 2.67, respectively.

Polyethylene (PE) fibers with the tensile strength, elastic modulus, and density of 3000 MPa, 100 GPa, and 0.97 g/cm^3 were used as the reinforcement in ECC materials. The fibers had a diameter of 24 μm and a length of 18 mm. It is noted that in the previous work of the authors [28], high-strength ECC with 18-mm PE fibers showed the highest tensile ductility. Since the binder system of this work was similar to that adopted in the previous work, 18-mm PE fibers were adopted here. Also, the PE fibers were not pre-treated for bond improvement in this study.

Polycarboxylate ether type super-plasticizer (MasterGlenium SKY8588) purchased from BASF Hong Kong was used in the HS-ECC mixing, and tap water in the laboratory was used in ECC production. The solid content of the super-plasticizer was 22% by weight.

2.2. Preparation and testing of GPA

The activator to precursor ratio was 0.08 and the water to precursor ratio was 0.30 by weight to produce artificial geopolymer fine aggregates. In terms of casting methods, one-part geopolymer mixing approach was adopted to maximize the feasibility of industrialization [32]. During the mixing, FA and solid activator were dry-mixed for the first 5 min, water was then added and the resultant slurry was stirred for another 5 min. Subsequently, the fresh pastes were poured into cubic molds (100 mm × 100 mm × 100 mm) and vibrated for 30 s to remove large air pores. After 24 h, demolding was conducted, and the specimens were crushed into fragments with a dimension smaller than 4.75 mm to meet the size requirement of fine aggregates. The fragments were then pre-heated in an oven with 105 °C for 24 h to reduce the drying shrinkage [39] and improve the early strength. Afterwards, they were kept in sealed plastic bags. It should be pointed out that the energy consumption and carbon emission during the crushing and heating of GPA are critical parameters of sustainability. It is believed that the reduction of natural resource depletion and waste landfills suffices to balance overall energy usage and greenhouse gas (GHG) emission in the GPA production and application.

Due to the extremely busy laboratory schedule, the produced GPA had already been stored for six months before they were used for ECC mixing. It is anticipated that the six-month sealed curing can guarantee a more complete pozzolanic reaction of GPA and thus make more stable aggregate characteristics. The particle size distribution of GPA and FSS is shown in Table 2 and the appearances of GPA and FSS are shown in Fig. 2. To assess the strength of geopolymer fine aggregates, six 20 mm × 20 mm × 20 mm cubes were produced following the above-mentioned mixing procedure, and the average compressive strength at 28 d was found to be 8.1 MPa. Here it is worth mentioning that the comparatively low activator-to-precursor ratio (0.08) in producing the GPA can achieve a strong flaw effect, tailor ECC manufacturing and improve environmental friendliness (i.e., use of less alkali activator).

The specific gravity of GPA was tested according to GB/T 14684–2011 [38], and the obtained value (2.09) was lower than that of fine silica sand (2.67). Because the common water absorption method was not accurate in testing lightweight fine aggregates with high water absorption [40], the paper towel method proposed by the Department of Transportation for the State of New York was specially adopted here for the water absorption test of geopolymer fine aggregates [41]. The obtained water absorption value of GPA was 22.3%.

2.3. Preparation of ECC

The mix proportions of five GPA replacement ratios (F100G0: 0%, F75G25: 25%, F50G50: 50%, F25G75: 75% and F0G100: 100%) are listed in Table 3, where "F" donates FSS and "G" represents GPA in the mix IDs. In order to highlight the effect of sand hybridization, the volume ratios of all the components were kept the same [including the volume ratio of total fine aggregates (FSS + GPA)]. The sand contents in Table 3 were calculated according to the tested specific gravity, and F100G0 was adopted as a control mix with the FSS/binder weight ratio of 0.25. The particle size distributions of the hybrid FSS and GPA in different mixes are presented in Table 2. Because of the high water absorption of GPA, both the FSS and GPA were pre-wetted to the saturated surface dry (SSD) condition before ECC casting. All the solid materials (i.e., cement, SF and SSD sand) were then dry-mixed in a mixer for 5 min. After that, the wet agents including water and super-plasticizer were added together and the mixture was stirred for another 10 min. It is noted that in Table 3, the super-plasticizer dosage means the mass of the solid content, and the water contained in the super-plasticizer has been calculated into the mass of the water used. After a uniform mortar was obtained, PE fibers were put into the mixer, and the mixture was continuously stirred for 5 min. Then, the fresh ECC mixture was casted into dumbbell molds (shown in Fig. 3) and 50 mm × 50 mm × 50 mm cubic molds, covered with a plastic sheet to prevent water evaporation. Next, the specimens were kept at the room temperature (23 °C) for 24 h, and then demolded. Before being kept in water (20 °C)

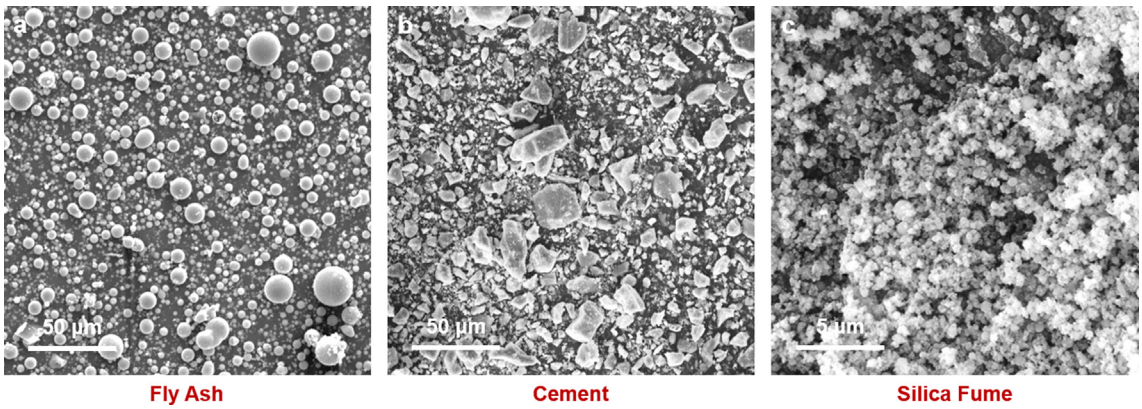

Fig. 1. SEM images of (a) fly ash, (b) cement, and (c) silica fume.

Table 2
Particle size distribution of GPA, FSS and hybrid sand in ECC.

Particle size (mm)	2.36–4.75	1.18–2.36	0.6–1.18	0.3–0.6	0.15–0.3	0–0.15
GPA	30.00%	28.00%	18.00%	6.00%	3.00%	15.00%
FSS	0.00%	0.00%	0.00%	21.00%	72.00%	7.00%
F100G0	0.00%	0.00%	0.00%	21.00%	72.00%	7.00%
F75G25	7.50%	7.00%	4.50%	17.25%	54.75%	9.00%
F50G50	15.00%	14.00%	9.00%	13.50%	37.50%	11.00%
F25G75	22.50%	21.00%	13.50%	9.75%	20.25%	13.00%
F0G100	30.00%	28.00%	18.00%	6.00%	3.00%	15.00%

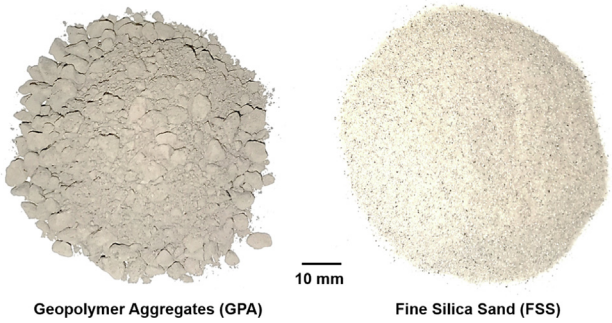

Fig. 2. Photographs of geopolymer fine aggregates and fine silica sand.

for 28 d curing, specimens were weighed with the demolding densities recorded, which are presented in Table 3. It can be seen that with the increasing replacement ratio of FSS by GPA, the ECC density became lower due to the lightweight nature of artificial GPA.

2.4. Testing methods

Three 50 mm × 50 mm × 50 mm cubes were tested under compression with the loading rate of 1.0 MPa/s for each mix, according to ASTM C109/C109M [42]. For the direct tensile test, three dumbbell specimens were tested for each mix proportion with the loading rate of 0.5 mm/min controlled by the crosshead of the testing machine. The clamp supports of both specimen ends were rotational and followed the recommendation of ECC tensile testing by van Zijl et al. [43]. During the testing procedure, a linear variable differential transformer (LVDT) was glued on one side of the specimens to obtain the tensile strain in the middle section, with the gauge length set as 80 mm (Fig. 3). On the other side, the digital image correlation (DIC) method [44,45] was used to measure the strain field in the central area of the specimens (Fig. 3). For specimen preparation, speckle pattern was sprayed on the targeted measuring side for DIC recognition. During the direct tensile test, a digital camera was adopted to take photographs of the central area at an interval of three seconds.

After the direct tensile test, samples where the fiber failure modes could be observed were carefully cut off from the fracture surface for SEM analysis. In a similar way, extra samples were also cut from the central part of the dumbbell specimens for microscopic analysis of the GPA, matrix, and GPA/matrix interface in the Backscattered-Electron (BSE) mode. The samples were fixed in epoxy resins and then polished to achieve a smooth surface. Both the SEM and BSE samples were coated with gold sputter before the tests, and the same device (Tescan VEGA3) was used for both tests.

Finally, small samples with enclosed tensile cracks were cut from the central part of the dumbbell specimens after direct tension. The samples were then scanned by a micro-focus X-ray CT system (YXLON FF35 CT) with the X-ray tube voltage of 140.0 kV and the X-ray Tube Current of 40 μA. The voxel size of the scanned CT images was 29.7 μm. The size distributions of flaws and GPA, as well as the cracking condition, were analyzed using ImageJ software.

3. Mechanical properties of HS-ECC

This section presents the test results of the mechanical properties of ECC with hybrid GPA and FSS, including the compressive strength (f'_c), tensile properties [strain capacity (ε_t), cracking strength (f_{to}), ultimate strength (f_t)], strain energy density (u) in tension, and average crack width (w_u) at the ultimate strain. Table 4 summarizes the mechanical properties of the tested five mixes of ECC, and Fig. 4 shows the corresponding tensile stress–strain curves. Detailed discussions on these properties are given in the sections below. It is noted that the dumbbell geometry with the thickness of 13 mm could have a positive effect on the tensile property of ECC due to the two-dimensional fiber orientation. The wall effect and possible troweling could even lead to dominant one-dimensional fiber orientation. In addition, the average crack width of the ECC was obtained along a central vertical line within the gauge length of the specimen from the digital photograph at the ultimate stage [43].

The addition of GPA lowered the compressive strength of HS-ECC because of the comparatively low strength of GPA compared with silica sand. Compared with F100G0 (152.7 MPa), the reduction ratios in compressive strength were 9.6%, 19.1%, 23.4%, and

Table 3
Mix proportions of ECC (kg/m^3).

Mix ID	F100G0	F75G25	F50G50	F25G75	F0G100
Cement	1267.6	1246.8	1233.4	1223.8	1221.6
Silica Fume	316.9	311.7	308.3	305.9	305.4
SSD FSS (Dry FSS)	396.1 (393.0)	293.0 (290.7)	192.7 (191.2)	96.4 (95.6)	0 (0)
SSD GPA (Dry GPA)	0 (0)	93.5 (76.5)	183.5 (150.0)	273.8 (223.9)	363.4 (297.1)
Water	248.8	244.7	242.1	240.2	239.7
Super-plasticizer (in solid)	20.6	20.3	20.0	19.9	19.9
PE Fiber (2% by vol.)	19.4	19.4	19.4	19.4	19.4
Demolding Density (g/cm^3)	2.25	2.21	2.18	2.16	2.15

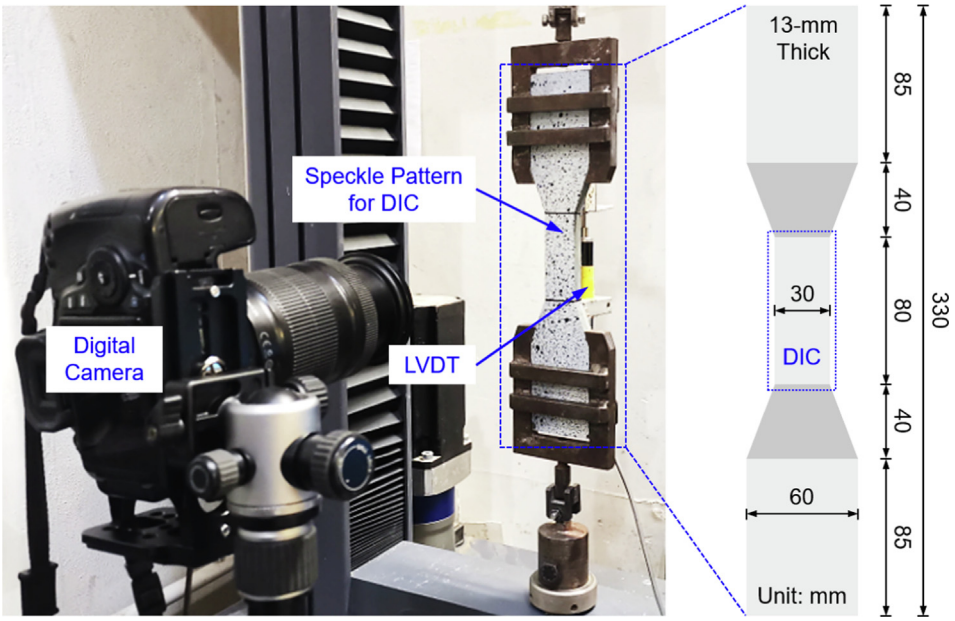

Fig. 3. Experimental setup and the geometory of the tensile specimen.

Table 4
Summary of mechanical properties of ECC with hybrid GPA and FSS.

Properties	F100G0	F75G25	F50G50	F25G75	F0G100
Compressive Strength, f'_c (MPa)	152.7 ± 3.9	138.1 ± 9.0	123.5 ± 3.4	117.0 ± 2.5	106.3 ± 5.9
Tensile Strain Capacity, ε_t (%)	2.6 ± 0.5	4.5 ± 0.9	5.6 ± 0.3	6.1 ± 0.2	7.2 ± 0.5
Ultimate Tensile Strength, f_t (MPa)	15.3 ± 1.0	12.5 ± 0.3	10.5 ± 0.4	9.0 ± 0.5	8.9 ± 0.2
Tensile Cracking Strength, f_{t0} (MPa)	11.6 ± 1.5	8.3 ± 0.5	5.9 ± 0.5	4.9 ± 0.3	4.0 ± 0.2
Average Crack Width at the Ultimate Strain, w_u (μm)	157.3 ± 36.2	119.3 ± 12.7	97.8 ± 2.6	90.3 ± 6.1	82.4 ± 4.0
Strain Energy Density, u (kJ/m^3)	425 ± 57	549 ± 75	607 ± 21	499 ± 37	646 ± 71
$f'_c f_t \varepsilon_t / w_u$ Index (MPa^2/μm)	0.39	0.65	0.74	0.71	0.83

30.4% for F75G25, F50G50, F25G75 and F0G100, respectively (Fig. 5**a**). However, the tensile strain capacities of F75G25 (4.5%), F50G50 (5.6%), F25G75 (6.1%), and F0G100 (7.2%) increased by 73%, 115%, 136%, and 178% compared to that of F100G0 (2.6%). Owing to the flaw effect, the use of GPA could lower the fracture toughness of the matrix and thus enhance the pseudo strain-hardening potential of ECC materials.

Tensile cracking strength, which reflects the matrix's fracture toughness to some extent, also decreased from 11.6 MPa to 4.0 MPa as the GPA ratio increased from 0% to 100% (Fig. 5**b**). In addition, during the direct tension, it was observed that the hardened tensile strength, i.e., the increments from the cracking strength to the ultimate strength $[(f_t - f_{t0})/f_{t0}]$, for F100G0, F75G25, F50G50, F25G75 and F0G100 were 32%, 50%, 79%, 84%, and 125%, respectively. In other words, the strain-hardening behavior of HS-ECC was significantly improved although the ultimate tensile strength decreased with the increasing GPA ratio. Also, it is known that the ultimate tensile strength of ECC is mainly determined by the fiber strength as well as the fiber/matrix bond. Therefore, the decrease in the ultimate tensile strength of ECC with higher GPA ratio is possibly due to the disturbed fiber distribution caused by the existence of GPA. In the future study, the above effect needs to be confirmed and further investigated.

Apart from the ultimate tensile strengths and strains of ECC as discussed above, the distinct strain-hardening phenomena could be directly observed in the tensile stress–strain relationships in Fig. 4. As shown in the figure, the strain-hardening behavior of ECC became more obvious with the increase of GPA ratio. In addition, when new cracks occurred, the stress drops in the strain-hardening part were large in F100G0, while for ECC with higher GPA ratios, the stress drops became less abrupt. The lower fluctuation of the stress–strain curves indicated an average tighter crack width generated in the direct tension of ECC with higher GPA replacement ratios [46]. In Table 4, the average crack widths of ECC mixes with higher GPA ratios tend to be smaller at the ultimate strain. It is indicated that the use of GPA leads to the increase in the number of cracks while improving the crack control ability of HS-ECC.

The strain energy density (u) in tension (Table 4) was also calculated based on the area under the tensile stress–strain curves of ECC (see the inset in Fig. 6**f**). With the higher ratio of GPA, the tensile strain energy density of ECC exhibited an increasing trend, indicating a more ductile and better energy-absorption ability of ECC. It is noted that the comparatively low strain energy density of F25G75 may be caused by the stochastic nature of tested specimens or compaction matter. In the following study, this phenomenon should be further investigated to find out the reason. As ECC incorporating higher ratios of GPA have lower tensile and compressive strengths but higher tensile strain capacity and smaller average crack width, the overall performance should be evaluated. Therefore, the four-paramter $f'_c f_t \varepsilon_t / w_u$ index [12] was calculated and presented in Table 4. It can be found that F0G100 recorded the highest the $f'_c f_t \varepsilon_t / w_u$ index (0.83 MPa^2/μm). All the mixes with the hybrid use of GPA and silica sand or pure GPA

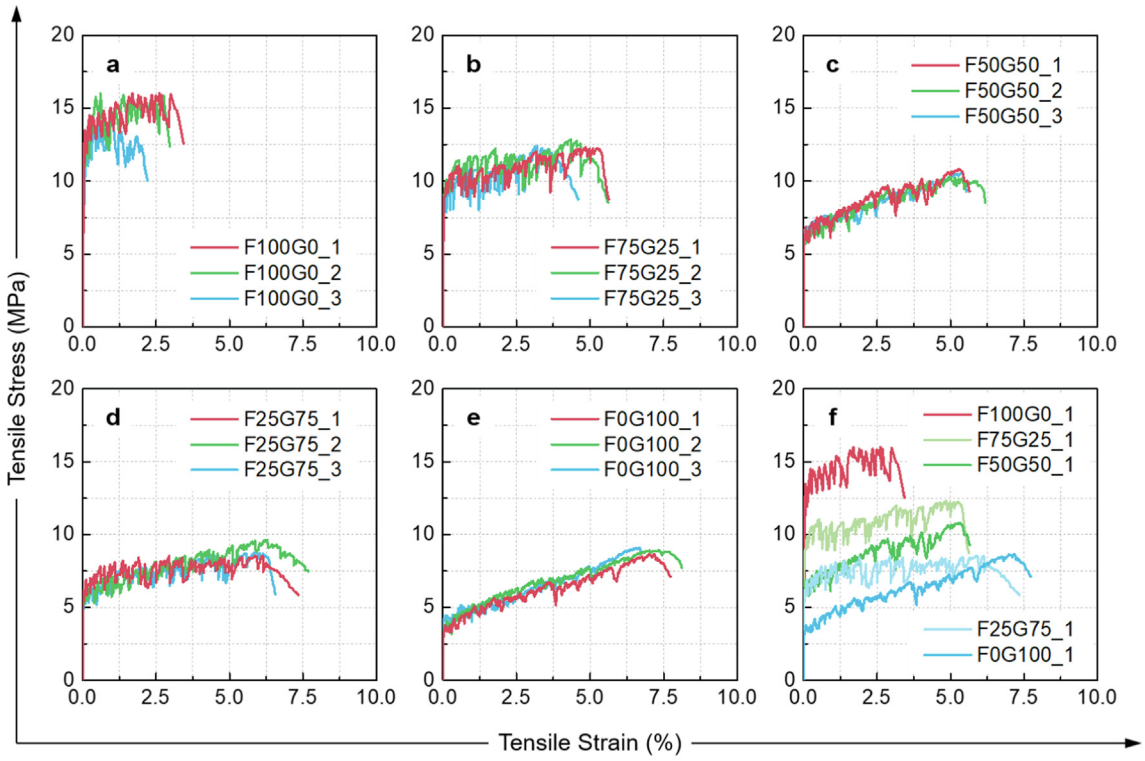

Fig. 4. Tensile stress–strain curves: (a) F100G0, (b) F75G25, (c) F50G50, (d) F25G75, (e) F0G100 and (f) comparison of different mixes. The smaller fluctuation of the stress–strain curves indicates an average tighter crack width generated in the direct tension of ECC with higher GPA replacement ratios.

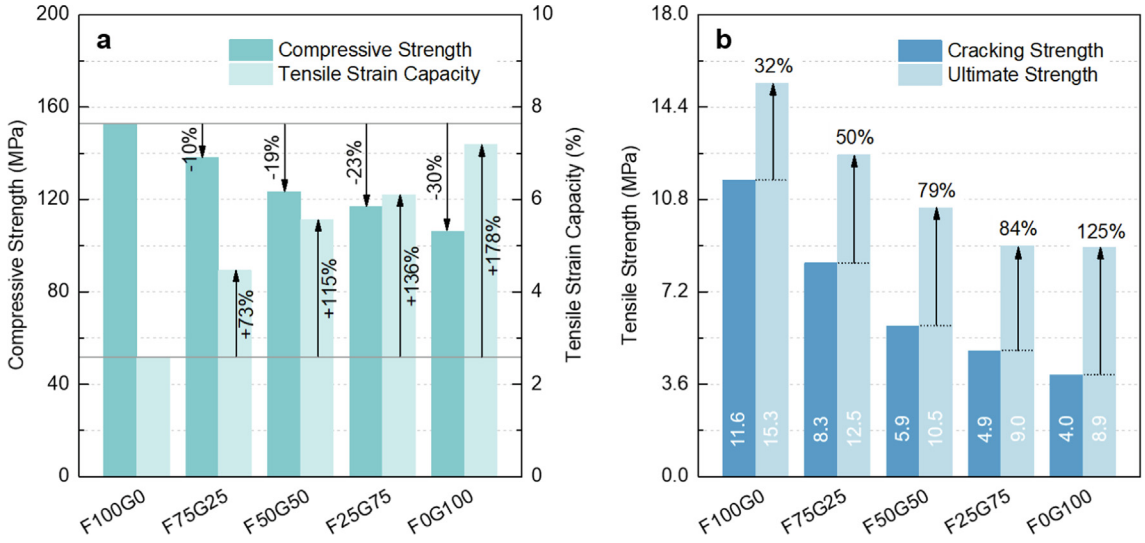

Fig. 5. Mechanical properties of ECC with hybrid GPA and FSS: (a) Compressive strength and tensile strain capacity, and (b) tensile cracking and ultimate strengths. Replacing FSS with GPA in ECC enhanced the tensile strain capacity and strain-hardening behavior, but decreased the compressive and tensile strengths.

exhibited higher index value than F100G0 which had fine silica sand alone as fine aggregates (0.39 $MPa^2/\mu m$). These results further demonstrated the positive role of artificial GPA in optimizing the overall performance of HS-ECC.

To tailor the mechanical performance of ECC by using hybrid FSS and GPA in future study, the relationships between the mechanical properties of ECC and the GPA replacement ratio were plotted and fitted, as shown in Fig. 6. The parameters including compressive strength, tensile strain capacity, ultimate tensile strength, tensile cracking strength, and average crack width all exhibited a linear variation with the replacement ratio change of GPA. The obtained correlation coefficients were no less than 0.94 ($r \geq 0.94$). Comparatively, the GPA-ratio-dependency of the strain energy density ($r = 0.71$) and the $f'_d f_t \varepsilon_t / w_u$ index ($r = 0.90$) was relatively weak. Nevertheless, it is highly feasible to tune the strength and ductility performance of HS-ECC for different application purposes through adjusting the GPA to FSS ratio and referring to the relationships as shown in Fig. 6.

As the maximum crack width is an important parameter for the assessment of concrete durability [47,48], its evolution under

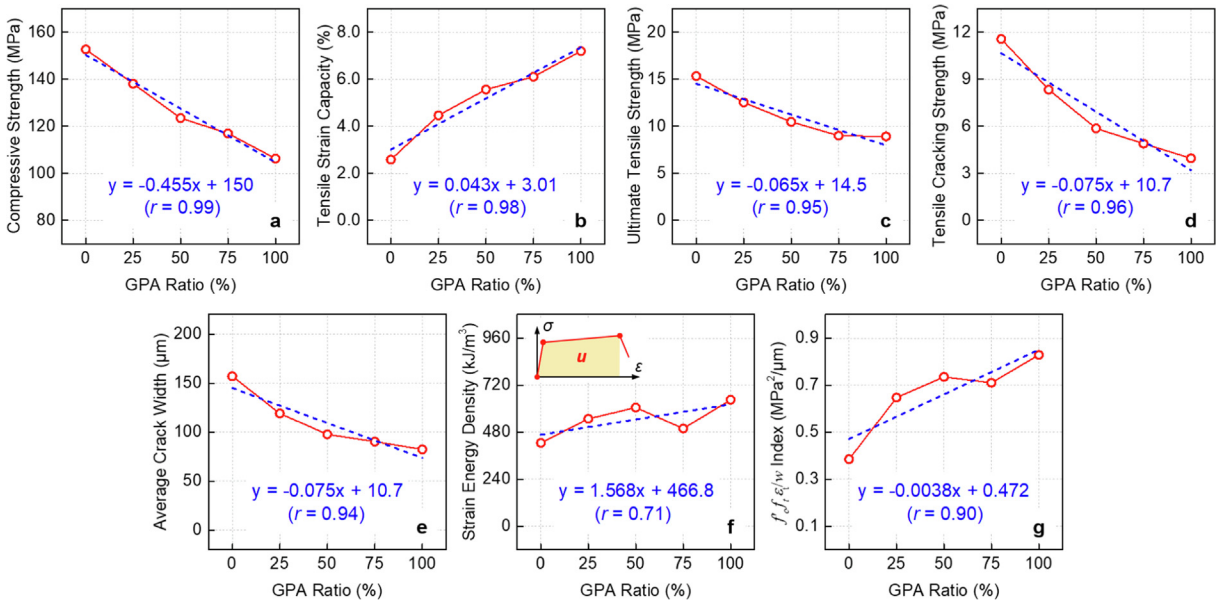

Fig. 6. Relationships between mechanical properties of ECC and GPA replacement ratio: (a) compressive strength, (b) tensile strain capacity, (c) ultimate tensile strength, (d) tensile cracking strength, (e) average crack width at the ultimate strain, (f) strain energy density, and (g) $f'_c f_t \varepsilon_t / w$ index. All the mechanical properties approximately showed a linear correlation with the GPA replacement ratio.

direct tension was analyzed. It is noted that the crack widths were also obtained along a central vertical line within the gauge length of the specimen based on the digital photographs (similar to the average crack calculation) [43], and the results are presented in Fig. 7. As the allowable crack width in standards or codes is usually 200–300 μm [49], it seems that the maximum crack widths of all the ECC mixes satisfied this requirement. In addition, although the maximum crack widths at the ultimate stage were not dependent on the GPA-to-FSS ratio, ECC with higher GPA ratios showed a gentler trend of the maximum crack width evolution. In other words, the maximum crack width at a fixed strain level decreased with a higher GPA-to-FSS ratio. It is indicated that GPA can also be used to tailor the durability performance of ECC materials.

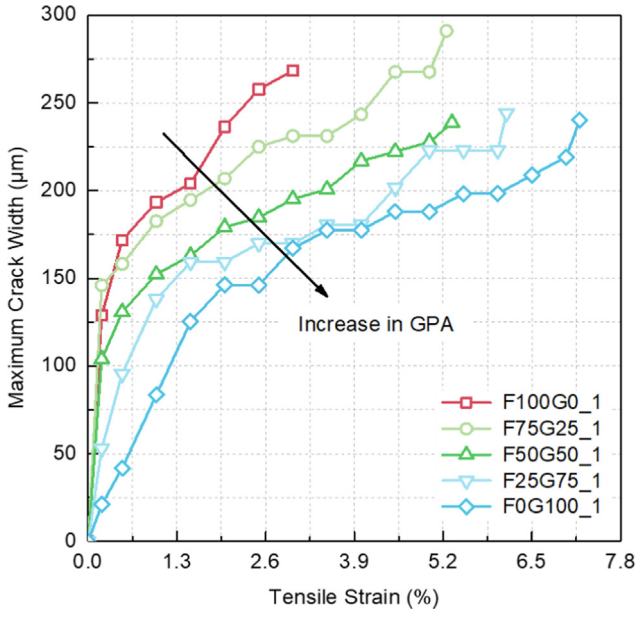

Fig. 7. Evolution of the maximum crack width of ECC with hybrid GPA and FSS. ECC with higher GPA ratio showed a smaller maximum crack width at the same tensile strain level.

4. Microscopic properties of HS-ECC

4.1. BSE analysis

Fig. 8 and Fig. 9 show the BSE images of GPA/matrix and FSS/-matrix interfaces, respectively. In Fig. 8**a**, the interface between GPA and the cementitious matrix was easy to be recognized, because many unreacted fly ash particles with a spherical shape could be found in the GPA region. The reason for the above phenomenon was that a low alkaline activator content (0.08) used for GPA production resulted in a comparatively inadequate alkali-activation degree. On the other hand, many unhydrated cement particles (in white) could be found interspersed in the cementitious matrix, which was caused by the low water-to-binder ratio in the mix design. In addition, PE fibers appeared as the black patterns in the BSE mode. Furthermore, an image with a magnification of 2000 times was captured (Fig. 8**b**), where a gel-like reaction zone with partially dissolved FA particles was observed in the GPA/matrix interface. It is mentioned that the above phenomenon only occurred in the contact area of the GPA/-matrix interface. Therefore, the gels in the interface reaction zone can be regarded as the products from the pozzolanic reaction between the calcium hydroxide provided by the cementitious paste and the unreacted FA particles [50].

From Fig. 9, no obvious reaction phenomenon was observed in the FSS/matrix interface location even from the image with the magnification of 4000 times, although the ion exchange between siliceous aggregates and the artificial cement solution was detected in the previous research [51]. In addition, a crack could be observed along the FSS/matrix interface due to the comparatively weak Van der Waals (VDW) force and frictional force in the FSS/matrix interface. In comparsion, no such crack was observed in the GPA/matrix interface as the reaction between unreacted FA and calcium hydroxide could generate extra chemical bond to enhance the GPA/matrix interface.

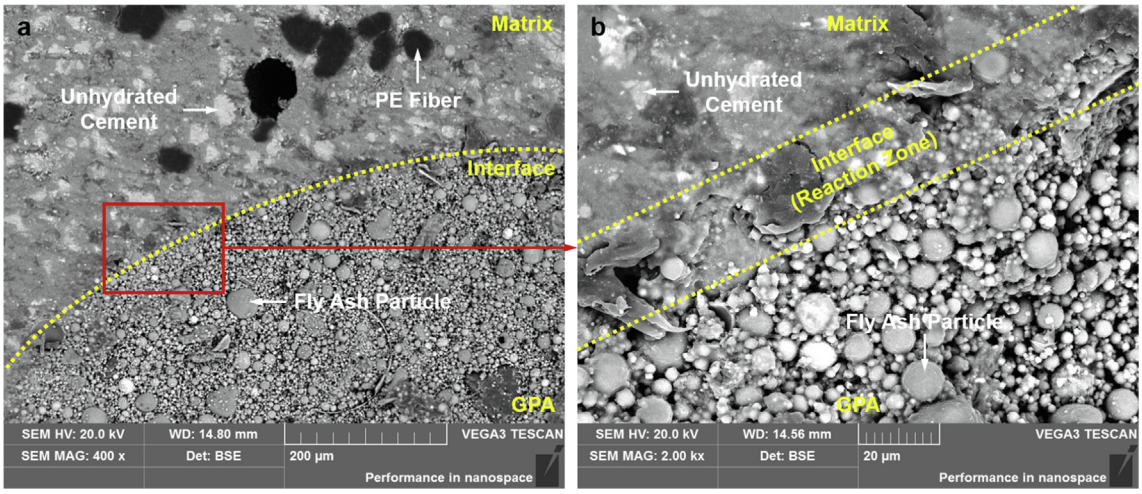

Fig. 8. BSE images of the GPA/matrix interface with a magnification of (a) 400 times and (b) 2000 times. A reaction zone is observed in the GPA/matrix interface where pozzolanic reaction occurs between the cementitious matrix and unreacted FA.

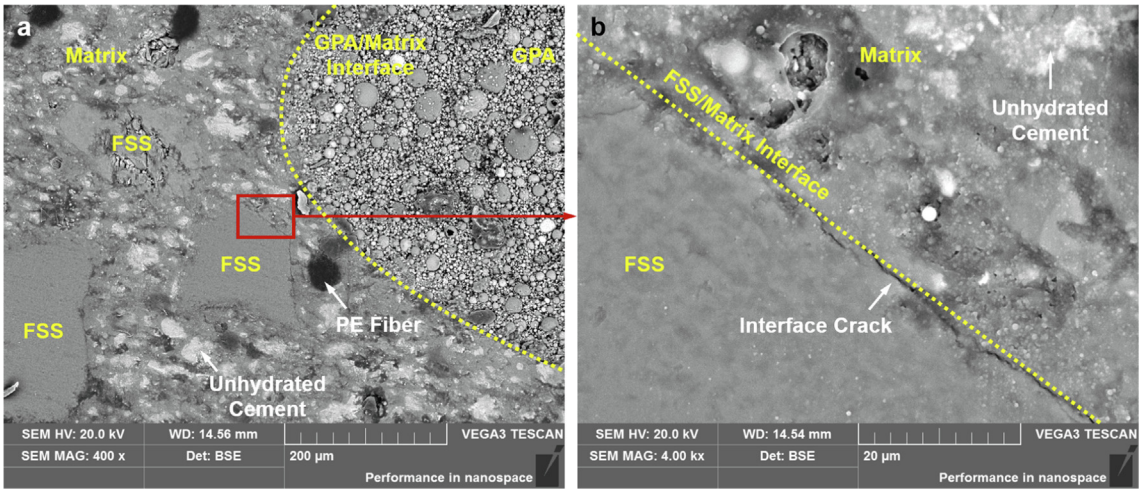

Fig. 9. BSE images of the FSS/matrix interface with a magnification of (a) 400 times and (b) 2000 times. No obvious reaction phenomenon but a crack is observed in the FSS/matrix interface.

4.2. SEM analysis for fiber failure modes

The strain-hardening behavior of ECC is highly dependent on the fiber status as well as the fiber–matrix bond. Fig. 10 shows the fiber failure conditions at the tensile fracture surface of F100G0, F50G50, and F0G100. As can be seen from the figure, both the pullout failure and the rupture failure modes were observed for all the samples. The rupture failure indicated a very strong fiber/-

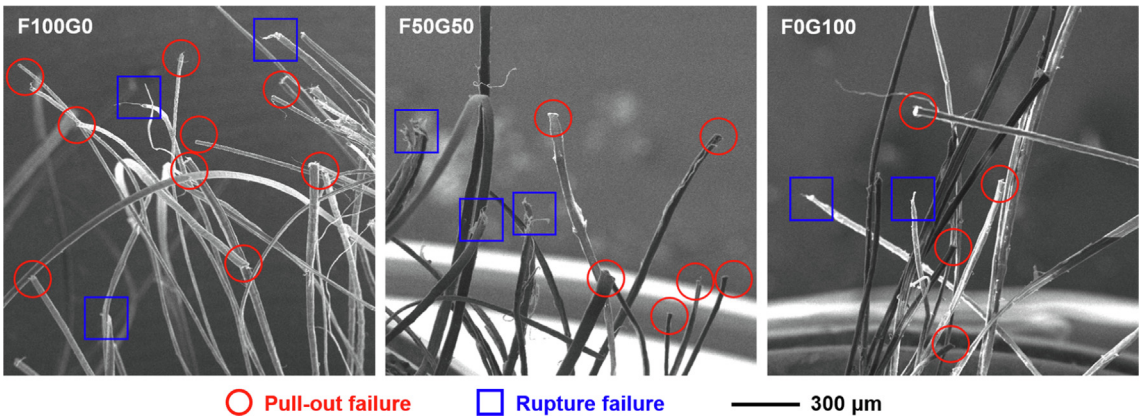

Fig. 10. SEM images of fiber failure modes: (a) F100G0, (b) F50G50, and (c) F0G100. Both rupture and pull-out failures of PE fibers can be observed for all the mixes.

matrix bond which would help sustain load but contribute less to the tensile ductility, while pull-out failure had the opposite effect. Therefore, partial rupture of the PE fibers in the ECC specimens could indicate an effective utilization of the fiber reinforcement in F100G0, F50G50, and F0G100. It is inferred that the fine aggregate type will not obviously influence the fiber failure modes of the produced ECC materials.

5. Cracking behavior

5.1. DIC analysis

Fig. 11 exhibits the strain fields and crack patterns of three significantly different types of HS-ECC specimens (i.e., F100G0, F50G50, and F0G100), which were obtained by the DIC method, at three different strain levels. Here, the first strain level (i.e., 0.2%) indicated the representative strain at the serviceability stage, the middle strain level represented the average of the first strain and the ultimate tensile strain, and the last strain level corresponded to the ultimate tensile strain. At the first strain level, F100G0 showed one localized crack with a comparatively large width. However, for F0G100, some uniformly distributed strain bands instead of visible cracking were observed because the cracks widths are too tight to be observed at 0.2% strain level. For F50G50, two light strain bands were found at the serviceability stage. At the last strain level, it was observed that the strain field of F100G0 showed several separated crack bands with the remaining regions less deformed. In comparsion, the cracking covered more areas for F50G50 with the reduced uncracked areas, and a uniform strain field occupied the whole gauge length of F0G100. It is clear that using GPA to replace FSS resulted in much more saturated multiple cracking and consequently the higher ductility of HS-ECC. In order to make a quantitative understanding of the cracking conditions, the cracking spacing analysis is conducted in the next section.

5.2. Crack spacing

The pseudo strain hardening (PSH) behavior of ECC is relevant to the stress transfer capacity of fibers, which is associated with the multiple-cracking phenomenon of this material. Generally speaking, the decrease in the crack spacing with an increase of the crack numbers represents a more saturated multiple-cracking condition. Based on the micromechanics of ECC considering the snubbing effect [52], the following equations of crack spacing [**Eq. (1–3)**] can be given:

$$x_d = \frac{L_f - \sqrt{L_f^2 - 2\pi L_f \psi x}}{2} \tag{1}$$

$$\psi = \frac{1+f^2}{e^{f\pi/2} - f} \tag{2}$$

$$x = \frac{(1-V_f)\sigma_m d_f}{4\tau_0 V_f} \tag{3}$$

where x_d represents the theoretical crack spacing for the condition of randomly distributed fibers in two dimensions; L_f, d_f, and V_f are the fiber length (18 mm), diameter (0.024 mm), and volume fraction (2%), respectively; f is the snubbing coefficient, which is found to be 0.59 for PE fiber (i.e., Ψ = 0.70) [53]; σ_m is the matrix cracking strength, which can take the value of f_{t0} in Table 4 for this study; and τ_0 is the fiber bond strength, which was found to be 1.52 MPa for PE fibers in high-strength cementitious matrix [53]. By introducing these parameters into **Eq. (1)**, the values of x_d in cases of F100G0, F75G25, F50G50, F25G75, and F0G100 were calculated as 2.94 mm, 1.99 mm, 1.35 mm, 1.11 mm, and 0.89 mm, respectively. It is indicated that ECC with lower matrix cracking strength tended to have smaller theoretical crack spacing. On the other hand, the tested average crack spacing (x_d^{test}) of F100G0, F75G25, F50G50, F25G75, and F0G100 were 6.07 mm, 2.67 mm, 1.76 mm, 1.48 mm, and 1.15 mm as directly recorded and calculated from the test. Based on the previous study of Kanda and Li [54], saturated multiple-cracking behavior can be achieved when x_d^{test} is located between x_d and $2x_d$. In other words, PSH intensity can be defined as **Eq. (4)**:

$$\text{PSH Intensity} = x_d^{test}/x_d \tag{4}$$

When PSH intensity ranges from 1.0 to 2.0, saturated cracking behavior can be obtained. Therefore, both the theoretical spacing (x_d and $2x_d$) and tested crack spacing (x_d^{test}) of all the mixes are plotted in Fig. 12 for a clearer comparison. As shown in the figure, only F100G0 cannot meet the requirement of saturated cracking criterion with the PSH Intensity of 2.06. For ECC with hybrid geopolymer and silica sand fine aggregates, even the 25% replacement of FSS by GPA could effectively reduce the PSH intensity from 2.06 to 1.34. The further increase of GPA ratio just resulted in a slight decreasing trend of the PSH intensity, which was further reduced by 0.05 (i.e., to 1.29) for ECC with full replacement of GPA (F0G100).

6. XCT analysis and flaw effect

6.1. Results of XCT analysis

Fig. 13 shows the representative 3D reconstructed XCT images of F100G0, F50G50 and F0G100. In order to make a clear visibility of different components in the samples, the dimension of

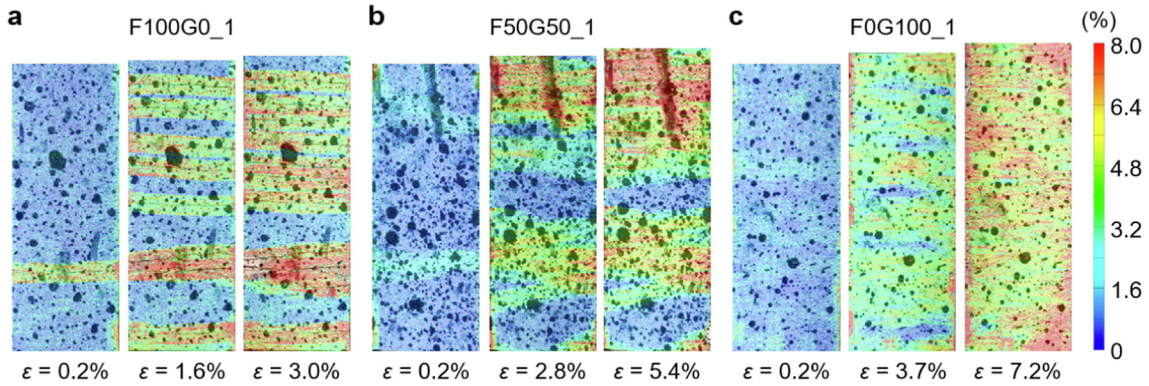

Fig. 11. Strain fields and crack patterns of ECC at different strain levels by obtained DIC analysis: (a) F100G0, (b) F50G50, and (c) F0G100. F0G100 shows the most uniform strain field, indicating a saturated cracking condition.

5 mm × 5 mm × 5 mm was chosen for the three mixes at the same grayscale level. As the scanned samples were cut from the fracture regions in the central parts of the specimens, tensile cracks could be observed for all the samples, which appeared approximately as a smooth surface. In comparison, initial flaws (pores) usually had a ballistic shape, while the remaining angular particles could be regarded as GPA.

Because of the existence of the penetrating multiple tensile cracks, it was hard to distinguish every initial flaw and GPA from the large-scale 3D images. Therefore, two-dimensional (2D) XCT images were used in this study to quantify the flaw effect (Fig. 14) as the area fractions of initial flaws and GPA in both 2D and 3D images can be regarded equal according to stereology principles [55,56]. From the 2D images, different components of ECC can be clearly distinguished, where the initial flaws were in black and GPA appeared in dark gray. In terms of the cracking patterns, more tensile cracks passing through the initial flaws and GPA could be observed from the mix proportions with higher GPA replacement ratios. It demonstrates the crack-activating role of GPA in the HS-ECC materials. Moreover, almost no cracks were observed along the interface between GPA and cementitious matrix, which further verified excellent bond at the GPA/matrix reaction zone as discussed in ***Section 4***.

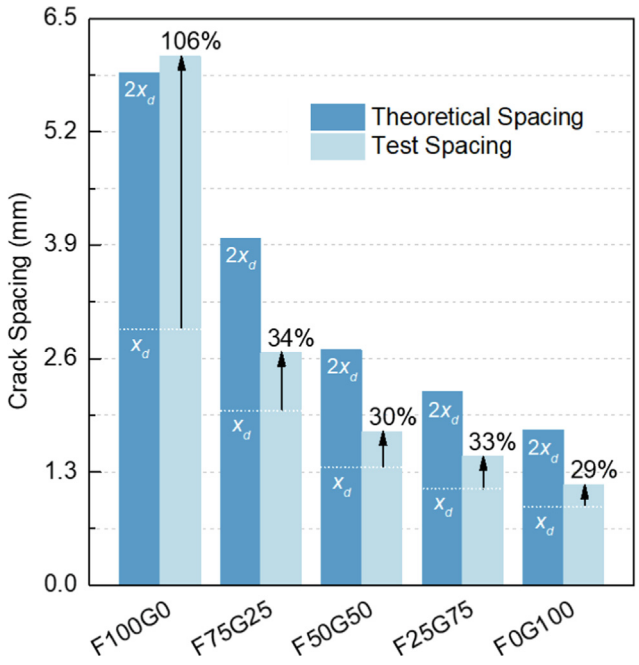

Fig. 12. Theoretical crack spacing and tested crack spacing for ECC with different GPA ratios. All the ECC mixes fully or partially incorporating GPA showed saturated multiple cracking behaviors (i.e., $x_d \le x_d^{test} \le 2x_d$).

6.2. Size distributions of initial flaws and GPAs

From the cracking patterns of HS-ECC, it can be observed that not all the initial flaws or GPA could actively function as the crack-inducing agents, and many of them still remained intact.

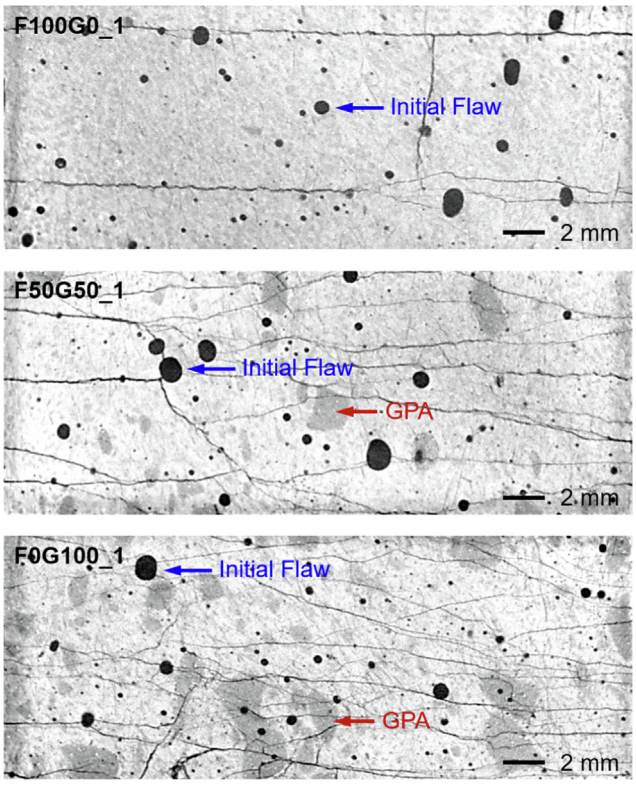

Fig. 14. 2D XCT images of F100G0, F50G50, and F0G100. Cracks tended to pass through the initial flaws and GPA, and more penetrating cracks could be observed for ECC with higher GPA replacement ratios.

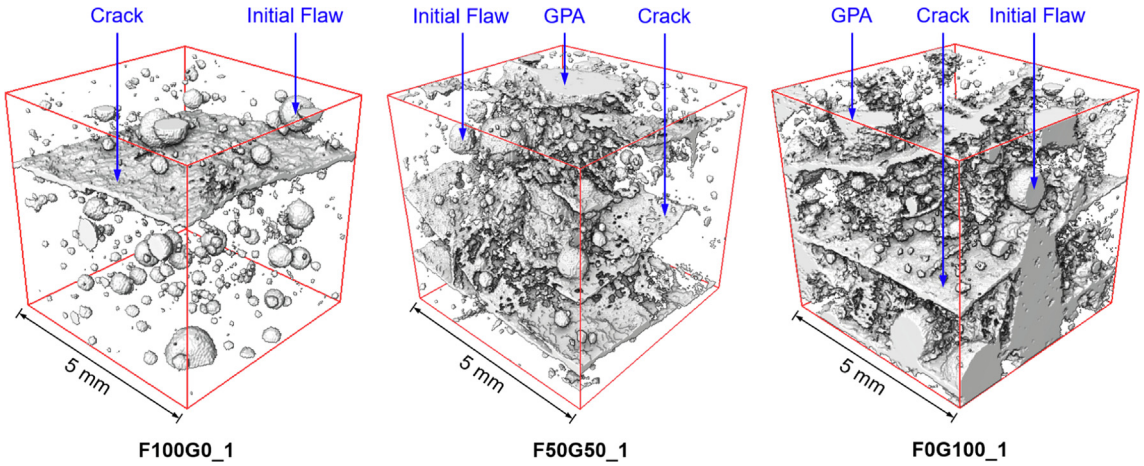

Fig. 13. 3D reconstructed XCT images of F100G0, F50G50 and F0G100. The tensile cracks, initial flaws, and GPA can be observed in the reconstructed 3D XCT images.

Therefore, behind the superficial phenomenon, the effectiveness of initial flaws and GPA should be evaluated as an important factor that determines the multi-cracking behavior of HS-ECC. In order to analyze the effectiveness of initial flaws and GPA in a more scientific way, both of them were further divided into two groups, i.e., inactive initial flaw (or inactive GPA flaw) and active initial flaw (or active GPA flaw). If there was at least one crack penetrating through the initial flaw (or GPA flaw), such initial flaw (or GPA flaw) could be treated as the active initial flaw (or active initial GPA), and the remaining intact initial flaws (or GPA flaws) were classified as inactive initial flaws (or inactive GPA flaws). Using ImageJ software, the equivalent radii and numbers of the inactive initial flaws, active initial flaws, inactive GPA flaws and active GPA flaws could be obtained from Fig. 14. It is noted that due to the limitation of resolution, the initial flaws (in black) with the radius smaller than 0.1 mm and GPA flaws (in dark gray, close to the gray matrix) with the radius smaller than 0.2 mm were not considered.

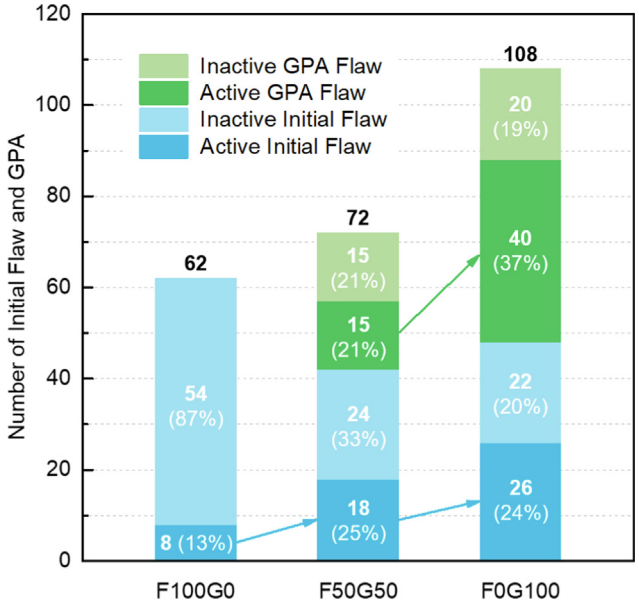

Fig. 15. Numbers of inactive GPA flaws, active GPA flaws, inactive initial flaws and active initial flaws in F100G0, F50G50 and F0G100. The addition of GPA made more initial flaws become active, and GPA flaws acted as a crack-inducing role in HS-ECC.

Based on the analysis results, the numbers of inactive GPA flaws, active GPA flaws, inactive initial flaws and active initial flaws in F100G0, F50G50, and F0G100 are shown in Fig. 15. From the figure, the initial flaw numbers were found to decrease when GPA flaws were partially or fully used in ECC casting because the total area of the cementitious paste decreased. However, the higher GPA replacement ratios contributed to the increase of the sum of initial flaws and GPA flaws. For flaw effectiveness, it can be observed that the active initial flaw number was eight for F100G0, went up to 18 for F50G50, and finally increased to 26 for F0G100. The active GPA flaw number showed a similar trend, which increased from 15 (F50G50) to 40 (F0G100) when the GPA ratio increased. Considering that GPA flaws could be regarded as additional flaws, the total active flaw (i.e., the sum of active initial flaws and GPA flaws) ratio was only 13% for F100G0, and very few cracks could be observed in the 2D XCT image as shown in Fig. 14. When GPA were added, the active total flaw ratio increased to 46% (F50G50) and 61% (F0G100), with more cracks generating and propagating through the initial flaws and GPA flaws.

Because the initial flaws were distributed dispersedly in the matrix with relatively small sizes, saturated cracks were hard to be induced in the matrix without GPA flaws due to the high matrix toughness in most regions. When GPA with low fracture toughness were used as the replacement of FSS, they would take up more areas in the matrix and reduce the matrix toughness more evenly. Because GPA had a good bonding with cementitious matrix, cracks would tend to propagate through GPA rather than along the GPA/-matrix interface. As new cracks generated in the regions with low fracture toughness, they were prone to propagate towards the area where more initial flaws and GPA flaws were located. Therefore, most of GPA flaws could work actively to induce cracks. In addition, the number of active initial flaws increased with the increase of the GPA replacement ratio.

Table 5
Cumulative distributions of the initial flaws and GPA flaws in ECC.

ECC	Function $F(r)$		Number N	Distribution Parameters			Correlation r
				λ	k	r_0	
F100G0	Initial Flaw	All: $F_{FT}(r)$	N_{FT} = 62	0.033	1.10	0.1	0.99
		Active: $F_{FE}(r)$	N_{FE} = 8	0.146	1.67	0.1	0.97
		Inactive: $F_{FI}(r)$	N_{FI} = 54	0.029	1.31	0.1	0.99
F50G50	Initial Flaw	All: $F_{FT}(r)$	N_{FT} = 42	0.032	0.90	0.1	0.99
		Active: $F_{FE}(r)$	N_{FE} = 18	0.059	0.87	0.1	0.98
		Inactive: $F_{FI}(r)$	N_{FI} = 24	0.021	1.00	0.1	0.99
	GPA Flaw	All: $F_{GT}(r)$	N_{GT} = 30	0.131	1.20	0.2	0.98
		Active: $F_{GE}(r)$	N_{GE} = 15	0.201	1.36	0.2	0.98
		Inactive: $F_{GI}(r)$	N_{GI} = 15	0.084	1.20	0.2	0.97
	Initial Flaw	All: $F_{FGT}(r)$	$N_{FGT} = N_{FT} + N_{GT}$	$F_{FGT}(r) = [N_{FT}F_{FT}(r) + N_{GT}F_{GT}(r)]/N_{FGT}$			0.99
	+	Active: $F_{FGE}(r)$	$N_{FGE} = N_{FE} + N_{GE}$	$F_{FGE}(r) = [N_{FE}F_{FE}(r) + N_{GE}F_{GE}(r)]/N_{FGE}$			0.98
	GPA Flaw	Inactive: $F_{FGI}(r)$	$N_{FGI} = N_{FI} + N_{GI}$	$F_{FGI}(r) = [N_{FI}F_{FI}(r) + N_{GI}F_{GI}(r)]/N_{FGI}$			0.98
F0G100	Initial Flaw	All: $F_{FT}(r)$	N_{FT} = 48	0.033	1.08	0.1	0.99
		Active: $F_{FE}(r)$	N_{FE} = 26	0.044	0.99	0.1	0.99
		Inactive: $F_{FI}(r)$	N_{FI} = 22	0.025	1.22	0.1	0.98
	GPA Flaw	All: $F_{GT}(r)$	N_{GT} = 60	0.137	1.07	0.2	0.99
		Active: $F_{GE}(r)$	N_{GE} = 40	0.210	1.14	0.2	0.99
		Inactive: $F_{GI}(r)$	N_{GI} = 20	0.070	1.49	0.2	0.99
	Initial Flaw	All: $F_{FGT}(r)$	$N_{FGT} = N_{FT} + N_{GT}$	$F_{FGT}(r) = [N_{FT}F_{FT}(r) + N_{GT}F_{GT}(r)]/N_{FGT}$			0.99
	+	Active: $F_{FGE}(r)$	$N_{FGE} = N_{FE} + N_{GE}$	$F_{FGE}(r) = [N_{FE}F_{FE}(r) + N_{GE}F_{GE}(r)]/N_{FGE}$			0.99
	GPA Flaw	Inactive: $F_{FGI}(r)$	$N_{FGI} = N_{FI} + N_{GI}$	$F_{FGI}(r) = [N_{FI}F_{FI}(r) + N_{GI}F_{GI}(r)]/N_{FGI}$			0.99

Note: r_0 is determined by the distinguishable minimum sizes of the initial flaws (r_0 = 0.1 mm) and GPA flaws (r_0 = 0.2 mm).

In order to analyze the size distributions of initial flaws, GPA flaws and total flaws (Initial flaws + GPA flaws), the Weibull-type function was used for the modeling [57]:

$$F(r) = 1 - \exp\left[-\left(\frac{\lambda}{r - r_0}\right)^k\right] \quad (5)$$

where $F(r)$ represents the cumulative probability of initial flaws, GPA flaws, or total flaws having an equivalent radius smaller than r, k represents the shape parameter, λ represents the scale parameter, and r_0 represents the smallest flaw radius. The initial flaws, GPA flaws, and total flaws were further divided into the active portion and the inactive portion, which were also modeled by **Eq. (5)**. The modeling results are listed in Table 5, and the fitting curves are plotted in Fig. 16. It can be seen from the table that **Eq. (5)** is suitable to fit the size distributions of initial flaws and GPA flaws as all the correlation coefficients are very close to 1. In addition, the total flaw distribution could be calculated based on the relevant equations and variables as listed in Table 5, and the modeling results also showed a good correlation with the experimental data.

6.3. Active initial flaws and GPA flaws

As the active initial flaws and active GPA flaws are related to the strain-hardening behavior of HS-ECC, the comparisons of total flaw and active total flaw distributions of F100G0, F50G50, and F0G100 are presented in Fig. 17. Both the cumulative distribution function (CDF) and probability density function (PDF) are plotted in the figure. In Fig. 17**a**, as the GPA ratio increased, the CDF curve moved right, indicating the increase of the total flaw size in the HS-ECC matrix. For the PDF curves, bimodal distributions were observed for ECC containing GPA (i.e., F50G50 and F0G100), which significantly differed from the unimodal distribution of initial flaws in F100G0 matrix. In addition, the PDF peaks of the total flaws of dif-

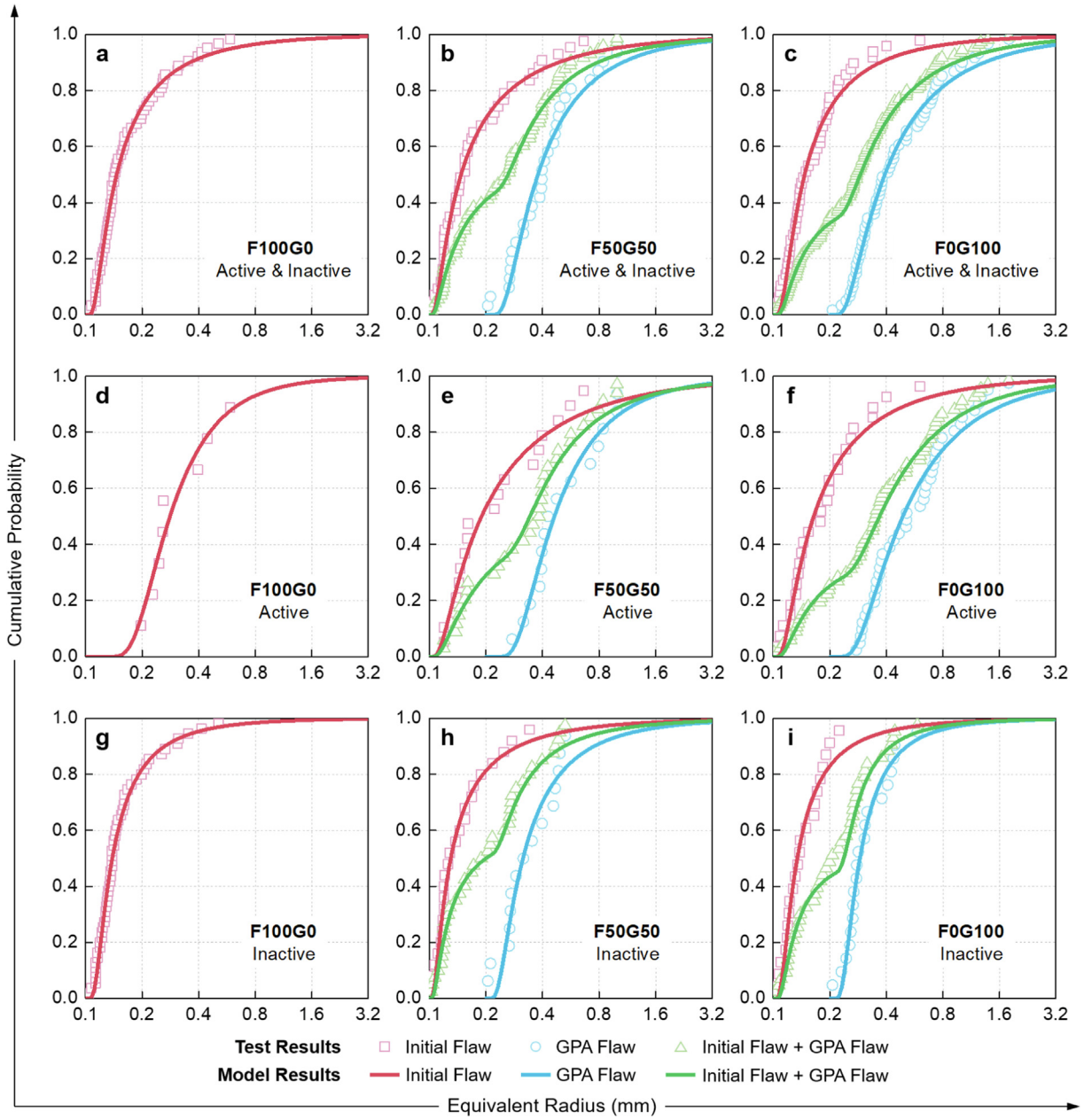

Fig. 16. Size distributions of initial flaws, GPA flaws, and total flaws in HS-ECC. The model results show good agreement with the test results.

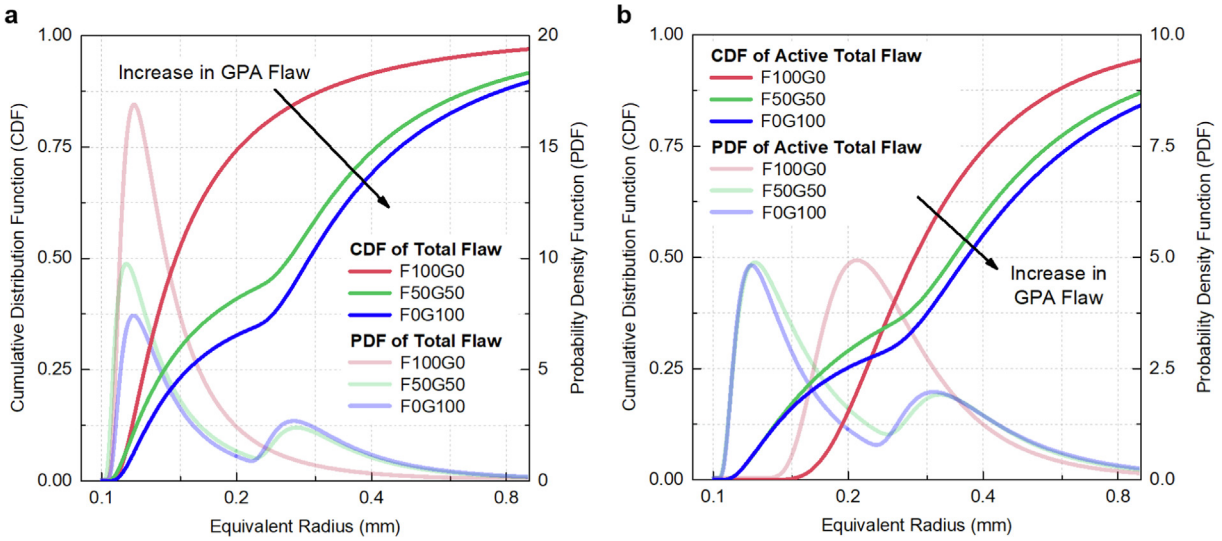

Fig. 17. Comparison of the cumulative distribution functions (CDF) and probability density functions (PDF) of (a) Total flaws (initial flaws + GPA flaws) and (b) Active total flaws (active initial flaws + active GPA flaws). GPA can be used to tailor the size distribution of the active total flaws in HS-ECC matrix.

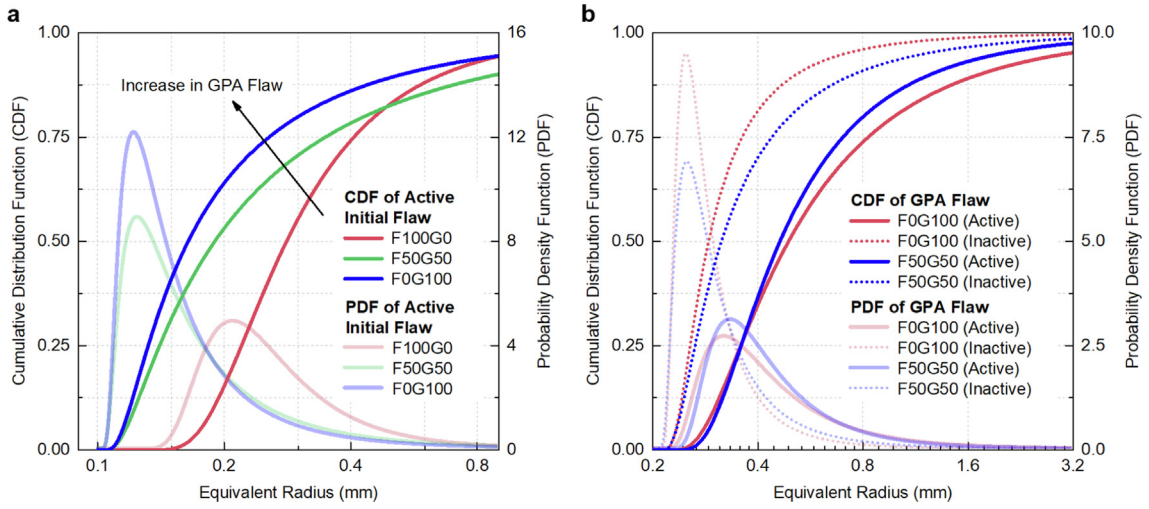

Fig. 18. Comparison of the cumulative distribution functions (CDF) and probability density functions (PDF) of (a) active initial flaws and (b) active and inactive GPA flaws. The size of acive initial flaws in the HS-ECC matrix significantly decreased with the use of GPA.

ferent mixes almost had similar equivalent radii, but the peak value decreased with the increase of GPA ratio. This phenomenon indicated that the initial flaw size distributions in the cementitious matrix were similar, but the addition of GPA would influence the total flaw size distribution curves. Interestingly, for the PDF of active total flaws in **Fig. 17b**, F100G0 had a lower peak intensity compared with the total flaw PDF curve in Fig. 17**a**, and the peak equivalent radius moved right, indicating that only the flaws with large radius (larger than 0.15 mm approximately) could be activated. However, when GPA were used as a partial or full replacement of FSS, the distributions of PDF and CDF curves of the active total flaws showed similar patterns with those of the total flaw conditions, although the second peak of the active total flaw PDF exhibited a bit larger peak radius than that of the total flaw PDF. It can be inferred here that the GPA with larger sizes were easier to be activated, and these aggregates could work better as the crack-inducing agents.

Fig. 18 presents the comparison of PDF and CDF curves of active initial flaws, active GPA flaws, and inactive GPA flaws of F100G0, F50G50, and F0G100. As mentioned above, the average equivalent radii of active initial flaws tended to decrease with the higher ratio of GPA replacement, indicating that more inactive initial flaws were turned into active initial flaws with the co-existence of GPA flaws. Therefore, it can be concluded that with the use of GPA, the size of active initial flaws in the HS-ECC matrix significantly decreased, as shown in Fig. 18**a**. At the meantime, as shown in Fig. 18**b**, ECC with full and partial contents of GPA showed similar PDF and CDF curves of active GPA flaws and inactive GPA flaws. In addition, a slightly increased size of active GPA flaws and decreased radius of inactive GPA flaws were found for F0G100 compared with F50G50.

7. Conclusions

In this study, hybrid geopolymer aggregates (GPA) and fine silica sand (FSS) were used to tailor the mechanical properties of high-strength engineered cementitious composites (HS-ECC). The mechanical properties and microstructures of the tailored ECC were investigated. In addition, the initial flaw and GPA flaw distributions were analyzed by XCT to explore the pseudo strain-

hardening (PSH) mechanisms of ECC with hybrid GPA and FSS. The main conclusions are drawn as follows.

- With a higher GPA-to-FSS replacement ratio, the tensile ductility, crack control, and energy absorption ability of HS-ECC could be enhanced, although the compressive strength and tensile strength were reduced. Generally the GPA replacement ratio had a linear influence on the mechanical properties of HS-ECC. Therefore, it is feasible to tailor ECC by adjusting the GPA ratio to achieve different combinations of strength and ductility for different types of applications.
- From the BSE analysis, a gel-like reaction zone with partially dissolved FA particles was observed in the GPA/matrix interface. It is indicated that pozzolanic reaction occurred between the calcium hydroxide provided by the cementitious paste and the unreacted FA particles from GPA. In addition, microcracks were observed in the FSS/matrix interface but not found in the GPA/matrix interface, indicating extra chemical bond was formed in the latter case that enhanced the interface.
- According to DIC results, ECC with higher GPA replacement ratios showed more saturated multiple-cracking behaviors. Crack spacing analysis supported this finding. The sole use of FSS in HS-ECC as fine aggregates may not meet the saturated cracking criterion, while only a 25% replacement of FSS by GPA could lead to the saturated multiple cracking.
- By introducing GPA, more inacive initial flaws were activated and became active in the matrix, which made the multiple-cracking of ECC more saturated. From the Weibull-based modeling results of initial flaws, GPA flaws, and total flaws (initial flaws + GPA flaws) distributions, it was observed that initial flaws with small sizes were gradually turned from "inactive" into "active" with higher GPA ratio. It was found that GPA could play a crack-inducing role during this procedure. Therefore, GPA tailored the active flaw size distributions in the HS-ECC matrix.

More information about GPA-based ECC materials can be found in the authors' previous work (feasibility study of GPA-ECC [33] and preliminary mechanism of GPA flaw effect [34]). In addition, it should be pointed out that the long-term performance is critical for the application of GPA-based ECC. The authors are also evaluating the long-term tensile performance of high-strength ECC incorporating GPA, and the results will be reported in the future.

CRediT authorship contribution statement

Ling-Yu Xu: Conceptualization, Methodology, Investigation, Formal analysis, Writing – original draft. **Bo-Tao Huang:** Conceptualization, Methodology, Investigation, Visualization, Writing – review & editing. **Jian-Cong Lao:** Investigation, Validation, Data curation. **Jian-Guo Dai:** Conceptualization, Funding acquisition, Supervision, Writing – review & editing.

Declaration of Competing Interest

The authors declare that they have no known competing financial interests or personal relationships that could have appeared to influence the work reported in this paper.

Acknowledgments

This study was supported by NSFC/RGC Joint Research Scheme (Project No. N_PolyU542/20), Chinese Guangdong Province R&D Plan for Key Areas (Project No. 2019B111107002), and The Hong Kong Polytechnic University through the Research Institute for Sustainable Urban Development (Project No. 1-BBWE). Ling-Yu Xu acknowledges the PhD studentship offered by The Hong Kong Polytechnic University. Bo-Tao Huang and Jian-Cong Lao would like to acknowledge the support by the Hong Kong Innovation and Technology Fund through the Research Talent Hub.

References

[1] V.C. Li, Engineered Cementitious Composites (ECC) - Bendable Concrete for Sustainable and Resilient Infrastructure, Verlag GmbH Germany, Springer, Berlin, Heidelberg, 2019.
[2] V.C. Li, On engineered cementitious composites (ECC) a review of the material and its applications, J. Adv. Concr. Technol. 1 (3) (2003) 215–230.
[3] E.H. Yang, Y. Yang, V.C. Li, Use of high volumes of fly ash to improve ECC mechanical properties and material greenness, ACI Mater. J. 104 (6) (2007) 620.
[4] V. Mechtcherine, O. Millon, M. Butler, K. Thoma, Mechanical behaviour of strain hardening cement-based composites under impact loading, Cem. Concr. Compos. 33 (1) (2011) 1–11.
[5] G.P.A.G. van Zijl, F.H. Wittmann, B.H. Oh, P. Kabele, R.D. Toledo Filho, E.M.R. Fairbairn, V. Slowik, A. Ogawa, H. Hoshiro, V. Mechtcherine, F. Altmann, M.D. Lepech, Durability of strain-hardening cement-based composites (SHCC), Mater. Struct. 45 (10) (2012) 1447–1463.
[6] I. Curosu, M. Liebscher, S. Burk, H. Li, S. Hempel, N. Raak, H. Rohm, V. Mechtcherine, Influence of fiber type on the tensile behavior of high-strength strain-hardening cement-based composites (SHCC) at elevated temperatures, Mater. Des. 198 (2021) 109397.
[7] B.T. Huang, Q.H. Li, S.L. Xu, W. Liu, H.T. Wang, Fatigue deformation behavior and fiber failure mechanism of ultra-high toughness cementitious composites in compression, Mater. Des. 157 (2018) 457–468.
[8] Q. Li, X. Yin, B. Huang, Y. Zhang, S. Xu, Strengthening of the concrete face slabs of dams using sprayable strain-hardening fiber-reinforced cementitious composites, Front. Struct. Civ. Eng. 16 (2) (2022) 145–160.
[9] R. Ranade, V.C. Li, M.D. Stults, W.F. Heard, T.S. Rushing, Composite properties of high-strength, high-ductility concrete, ACI Mater. J. 110 (4) (2013).
[10] Z. Zhang, A. Yuvaraj, J. Di, S. Qian, Matrix design of light weight, high strength, high ductility ECC, Constr. Build. Mater. 210 (2019) 188–197.
[11] D.-Y. Yoo, T. Oh, M.-C. Kang, M.-J. Kim, H.-J. Choi, Enhanced tensile ductility and sustainability of high-strength strain-hardening cementitious composites using waste cement kiln dust and oxidized polyethylene fibers, Cem. Concr. Compos. 120 (2021) 104030.
[12] B.-T. Huang, J.-X. Zhu, K.-F. Weng, V.C. Li, J.-G. Dai, Ultra-high-strength engineered/strain-hardening cementitious composites (ECC/SHCC): material design and effect of fiber hybridization, Cem. Concr. Compos. 129 (2022) 104464.
[13] K. Wille, A.E. Naaman, S. El-Tawil, G.J. Parra-Montesinos, Ultra-high performance concrete and fiber reinforced concrete: achieving strength and ductility without heat curing, Mater. Struct. 45 (3) (2012) 309–324.
[14] R. Yu, P.H.J.H. Spiesz, H.J.H. Brouwers, Development of an eco-friendly Ultra-High Performance Concrete (UHPC) with efficient cement and mineral admixtures uses, Cem. Concr. Compos. 55 (2015) 383–394.
[15] Z. Wu, C. Shi, W. He, D. Wang, Static and dynamic compressive properties of ultra-high performance concrete (UHPC) with hybrid steel fiber reinforcements, Cem. Concr. Compos. 79 (2017) 148–157.
[16] J.-C. Lao, L.-Y. Xu, B.-T. Huang, J.-G. Dai, S.P. Shah, Strain-hardening Ultra-High-Performance Geopolymer Concrete (UHPGC): matrix design and effect of steel fibers, Compos. Commun. 30 (2022) 101081.
[17] J.W. Bang, G. Ganesh Prabhu, Y.I. Jang, Y.Y. Kim, Development of ecoefficient engineered cementitious composites using supplementary cementitious materials as a binder and bottom ash aggregate as fine aggregate, Int. J. Polymer Sci. 2015 (2015) 1–12.
[18] X. Huang, R. Ranade, W. Ni, V.C. Li, Development of green engineered cementitious composites using iron ore tailings as aggregates, Constr. Build. Mater. 44 (2013) 757–764.
[19] X. Huang, R. Ranade, Q. Zhang, W. Ni, V.C. Li, Mechanical and thermal properties of green lightweight engineered cementitious composites, Constr. Build. Mater. 48 (2013) 954–960.
[20] A. Adesina, S. Das, Evaluation of the durability properties of engineered cementitious composites incorporating recycled concrete as aggregate, J. Mater. Civ. Eng. 33 (2) (2021) 04020439.
[21] J. Li, E.H. Yang, Macroscopic and microstructural properties of engineered cementitious composites incorporating recycled concrete fines, Cem. Concr. Compos. 78 (2017) 33–42.
[22] S. Subedi, G.A.A. Amador, H. Noorvand, M.M. Hassan, L. Mohammad, Evaluation of Raw Bagasse Ash as Sand Replacement for the Production of Engineered Cementitious Composites, in: Tran-SET 2020, American Society of Civil Engineers, Reston, VA, 2021, pp. 237–246.
[23] A. Adesina, S. Das, Mechanical performance of engineered cementitious composite incorporating glass as aggregates, J. Cleaner Prod. 260 (2020) 121113.
[24] H. Siad, M. Lachemi, M. Sahmaran, H.A. Mesbah, K.M. Anwar Hossain, A. Ozsunar, Potential for using recycled glass sand in engineered cementitious composites, Mag. Concr. Res. 69 (17) (2017) 905–918.

[25] A. Al-Fakih, B.S. Mohammed, M.S. Liew, On Rubberized Engineered Cementitious Composites (R-ECC): a review of the constituent material, Case Stud. Constr. Mater. 14 (2021) e00536.
[26] A. Adesina, S. Das, Performance of engineered cementitious composites incorporating crumb rubber as aggregate, Constr. Build. Mater. 274 (2021) 122033.
[27] Y. Li, X. Guan, C. Zhang, T. Liu, Development of high-strength and high-ductility ECC with saturated multiple cracking based on the flaw effect of coarse river sand, J. Mater. Civ. Eng. 32 (11) (2020) 04020317.
[28] B.-T. Huang, J.-Q. Wu, J. Yu, J.-G. Dai, C.K.Y. Leung, V.C. Li, Seawater sea-sand engineered/strain-hardening cementitious composites (ECC/SHCC): Assessment and modeling of crack characteristics, Cem. Concr. Res. 140 (2021) 106292.
[29] B.T. Huang, Y.T. Wang, J.Q. Wu, J. Yu, J.G. Dai, C.K. Leung, Effect of fiber content on mechanical performance and cracking characteristics of ultra-high-performance seawater sea-sand concrete (UHP-SSC), Adv. Struct. Eng. 24 (6) (2021) 1182–1195.
[30] S. İpek, O.A. Ayodele, K. Mermerdaş, Influence of artificial aggregate on mechanical properties, fracture parameters and bond strength of concretes, Constr. Build. Mater. 238 (2020) 117756.
[31] P. Ren, T.C. Ling, K.H. Mo, Recent advances in artificial aggregate production, J. Cleaner Prod. 125215 (2020).
[32] L.-Y. Xu, L.-P. Qian, B.-T. Huang, J.-G. Dai, Development of artificial one-part geopolymer lightweight aggregates by crushing technique, J. Cleaner Prod. 315 (2021) 128200.
[33] L.-Y. Xu, B.-T. Huang, J.-G. Dai, Development of engineered cementitious composites (ECC) using artificial fine aggregates, Constr. Build. Mater. 305 (2021) 124742.
[34] L.-Y. Xu, B.-T. Huang, V.C. Li, J.-G. Dai, High-strength high-ductility Engineered/Strain-Hardening Cementitious Composites (ECC/SHCC) incorporating geopolymer fine aggregates, Cem. Concr. Compos. 125 (2022) 104296.
[35] V.C. Li, D.K. Mishra, H.C. Wu, Matrix design for pseudo-strain-hardening fibre reinforced cementitious composites, Mater. Struct. 28 (10) (1995) 586–595.
[36] G.P.A.G. Van Zijl, The role of aggregate in high performance fibre reinforced cement-based composites, Concrete/Beton J. Concrete Soc. Southern Africa, Nr 110 (2005) 7–13.
[37] ASTM C618 – 19, Standard Specification for Coal Fly Ash and Raw or Calcined Natural Pozzolan for Use in Concrete, ASTM International, West Conshohocken, PA, 2019.
[38] GB/T 14684-2011, Sand for construction, Standardization Administration of People's Republic of China, Beijing, China, 2011. (in Chinese)
[39] A. Castel, S.J. Foster, T. Ng, J.G. Sanjayan, R.I. Gilbert, Creep and drying shrinkage of a blended slag and low calcium fly ash geopolymer Concrete, Mater. Struct. 49 (5) (2016) 1619–1628.
[40] J. Castro, L. Keiser, M. Golias, J. Weiss, Absorption and desorption properties of fine lightweight aggregate for application to internally cured concrete mixtures, Cem. Concr. Compos. 33 (10) (2011) 1001–1008.
[41] Test method No.: NY 703-19 E, Moisture content of lightweight fine aggregate, New York State Department of Transportation, Materials Bureau: Albany, NY, 2008.
[42] ASTM C109/C109M, Standard Test Method for Compressive Strength of Hydraulic Cement Mortars, ASTM International, West Conshohocken, PA, 2013.
[43] G.P. van Zijl, V. Slowik, R.D. Toledo Filho, F.H. Wittmann, H. Mihashi, Comparative testing of crack formation in strain-hardening cement-based composites (SHCC), Mater. Struct. 49 (4) (2016) 1175–1189.
[44] Q.-H. Li, X. Yin, B.-T. Huang, A.-M. Luo, Y. Lyu, C.-J. Sun, S.-L. Xu, Shear interfacial fracture of strain-hardening fiber-reinforced cementitious composites and concrete: a novel approach, Eng. Fract. Mech. 253 (2021) 107849.
[45] K.-D. Peng, B.-T. Huang, L.-Y. Xu, R.-L. Hu, J.-G. Dai, Flexural strengthening of reinforced concrete beams using geopolymer-bonded small-diameter CFRP bars, Eng. Struct. 256 (2022) 113992.
[46] M. Xu, S. Song, L. Feng, J. Zhou, H. Li, V.C. Li, Development of basalt fiber engineered cementitious composites and its mechanical properties, Constr. Build. Mater. 266 (2021) 121173.
[47] S.C. Paul, G.P. van Zijl, Chloride-induced corrosion modelling of cracked reinforced SHCC, Arch. Civ. Mech. Eng. 16 (4) (2016) 734–742.
[48] S.C. Paul, G.P. van Zijl, A.J. Babafemi, M.J. Tan, Chloride ingress in cracked and uncracked SHCC under cyclic wetting-drying exposure, Constr. Build. Mater. 114 (2016) 232–240.
[49] ACI 318-14, Building code requirements for structural concrete and commentary, American Concrete Institute, Detroit, Michigan, 2011.
[50] S. Hanehara, F. Tomosawa, M. Kobayakawa, K. Hwang, Effects of water/powder ratio, mixing ratio of fly ash, and curing temperature on pozzolanic reaction of fly ash in cement paste, Cem. Concr. Res. 31 (1) (2001) 31–39.
[51] W.A. Tasong, J.C. Cripps, C.J. Lynsdale, Aggregate-cement chemical interactions, Cem. Concr. Res. 28 (7) (1998) 1037–1048.
[52] H.C. Wu, V.C. Li, Snubbing and bundling effects on multiple crack spacing of discontinuous random fiber-reinforced brittle matrix composites, J. Am. Ceram. Soc. 75 (12) (1992) 3487–3489.
[53] R. Ranade, V.C. Li, M.D. Stults, T.S. Rushing, J. Roth, W.F. Heard, Micromechanics of high-strength, high-ductility concrete, ACI Mater. J. 110 (4) (2013) 375.
[54] T. Kanda, V.C. Li, Multiple cracking sequence and saturation in fiber reinforced cementitious composites, Concrete Res. Technol. 9 (2) (1998) 457–468.
[55] E. Underwood, Quantitative Stereology, Reading Addison-Wesley Publishing Co., Boston, MA, USA, 1970.
[56] M. Nedeljković, B. Ghiassi, G. Ye, Role of curing conditions and precursor on the microstructure and phase chemistry of alkali-activated fly ash and slag pastes, Materials 14 (8) (2021) 1918.
[57] H.C. Wu, V.C. Li, Stochastic process of multiple cracking in discontinuous random fiber reinforced brittle matrix composites, Int. J. Damage Mech. 4 (1) (1995) 83–102.